

# Encoding protein dynamic information in graph representation for functional residue identification

Yuan Chiang<sup>†</sup>, Wei-Han Hui<sup>†</sup>, and Shu-Wei Chang<sup>\*†,‡</sup>

<sup>†</sup>*Department of Civil Engineering, National Taiwan University, Taipei, Taiwan*

<sup>‡</sup>*Department of Biomedical Engineering, National Taiwan University, Taipei, Taiwan*

December 23, 2021

Recent advances in protein function prediction exploit graph-based deep learning approaches to correlate the structural and topological features of proteins with their molecular functions. However, proteins *in vivo* are not static but dynamic molecules that alter conformation for functional purposes. Here we apply normal mode analysis to native protein conformations and augment protein graphs by connecting edges between dynamically correlated residue pairs. In the multilabel function classification task, our method demonstrates a remarkable performance gain based on this dynamics-informed representation. The proposed graph neural network, ProDAR, increases the interpretability and generalizability of residue-level annotations and robustly reflects structural nuance in proteins. We elucidate the importance of dynamic information in graph representation by comparing class activation maps for the hMTH1, nitrophorin, and SARS-CoV-2 receptor binding domain. Our model successfully learns the dynamic fingerprints of proteins and provides molecular insights into protein functions, with vast untapped potential for broad biotechnology and pharmaceutical applications.

**Keywords:** Protein, Normal Mode Analysis, Function Prediction, Dynamics, Graph Neural Networks (GNNs), Deep Learning

---

\*changsw@ntu.edu.tw

Proteins are molecular machines that carry out a variety of functions in biological processes. From 1D sequences to 3D structures, the genetic codes determine the sequence of amino acids and the way proteins fold into 3D structures (Fig. 1a). With great experimental efforts, *e.g.* with X-ray crystallography (XRC) and cryogenic electron microscopy (cryo-EM), many protein structures have been determined at high resolutions, typically spanning from 1 to 4 Å<sup>1-4</sup>. To date, over 170,000 entries of 3D protein structures can be found in the Protein Data Bank (PDB)<sup>5</sup>, the repository of experimentally determined 3D structures of proteins, nucleic acids, and complex assemblies. However, the number of available protein structures falls far short of the available sequence data. For example, UniProt Knowledge-base (UniProtKB)<sup>6</sup>, the database of protein sequence and function, contains over 200 million annotated sequences.

To fill the gap between sequence and structure data and hence explore the unknown functions of newly discovered proteins, the determination of protein structures by experimental and computational techniques has been a long-standing issue in structural biology. Homology-modeling techniques have driven advances in the comparative construction and evaluation of protein structures<sup>7,8</sup>. Comparative construction means such homology-modeling techniques need *a priori* structures as templates to build the models, which inevitably limits the generalizability toward the large proportion of completely unknown structures. The recent development of deep learning methods takes advantage of an increasing amount of sequence data to predict 3D protein structure. In the 14th biennial Critical Assessment of Structure Prediction (CASP14), deep learning models AlphaFold2<sup>9</sup> and RoseTTAFold<sup>10</sup> achieved supremacy in the accuracy of blind structure prediction tests. At the frontier of deep learning approaches, both models took input from multiple sequence alignments (MSA) and applied attention-based message passing schemes on residue pairs. In particular, their integration with roto-translationally equivalent SE(3)-transformer and invariant point attention<sup>11,12</sup> plays a crucial role in the fine adjustment of torsional angles in backbones and side chains. With the aid of the high-throughput structures predicted by these models, we can now tackle the next challenge in protein function prediction by data-driven approaches.

In recent decades, there has been an emerging paradigm that, in proteins, *sequence-encodes-structure-encodes-dynamics-encodes-function*<sup>13</sup> (Fig. 1a). With the structures determined, the dynamics in turn regulate the behaviors and functions of proteins. For example, human MutT homolog 1 (hMTH1), as shown in Fig. 1b, utilizes different conformations of the same substrate binding pocket to recognize different types of oxidized nucleotides (8-oxo-dGTP and 2-oxo-dATP) and to conduct nucleotide saniti-

zation<sup>14</sup>. In many cases, protein functions are intertwined with dynamic properties ranging from local residues to global collective motions. More essentially, the functional prediction of proteins is a great challenge, and the problems are multifold. Traditional machine learning classifiers, such as support vector machines, random forests, and gradient boosted decision trees, have been extensively used to predict site-specific or protein-level functions<sup>15,16</sup>. Many of the recent deep learning models focus on the variations in sequence embedding and neural network architecture<sup>17–20</sup>. One of the most natural choices for learning protein features is the graph neural network (GNN). GNNs can aggregate local residue features in a high-dimensional space and learn appropriate representations for local and global inferences<sup>19</sup>. Although previous works demonstrate the utility of GNNs for protein function prediction, the dynamic properties of proteins have not been considered in most of these models. Even a tiny point mutation in the protein sequence or excess thermal overflow can distort the backbone structure, alter the dynamic behavior, and eventually nullify certain functions as a whole. It is therefore expected that encoding dynamic information of proteins into GNNs would increase the discriminatory capacity of neural networks for either regular function prediction or anomaly (for example, mutation) detection.

In this work, we propose a framework to incorporate dynamic information into graph-based deep neural networks. By processing protein structures into three feature pipelines, including spatial, topological, and dynamic features, we successfully increase the discriminatory power of neural networks and enhance the classification performance on protein function prediction. We retrieve 3D structures of proteins from PDB<sup>5,21–24</sup> and perform multilabel classification on molecular function (MF) gene ontology (GO) annotations obtained from Structure Integration with Function, Taxonomy, and Sequence (SIFTS) database<sup>21,25,26</sup>. We also use the gradient-weighted class activation map (Grad-CAM)<sup>27</sup> to identify the dynamically activated residues (DARs) by comparing the activation maps with and without dynamic information. Our model, protein dynamically activated residue (ProDAR), determines the residues that are critical to protein dynamic behaviors and that have fundamental importance for protein and drug engineering. We also demonstrate several examples of DARs identified by neural networks and discuss their effects on the dynamic characteristics of protein functions.



# Results

## ProDAR encodes the dynamic information of proteins in graph representation

Proteins *in vivo* are neither static nor rigid bodies but dynamic and deformable molecules undergoing conformational changes due to thermal fluctuations. Via exploration by thermodynamical process, particular atomistic configurations are sampled in large conformational space to obtain the desired behaviors. To screen thousands of conformational changes in a high-throughput manner, we apply normal mode analysis (NMA) to the anisotropic network model (ANM), a surrogate model where molecular structures are represented as bead-spring networks. As illustrated in Fig. 1c,  $C^\alpha$  atoms are extracted from the polypeptide chain as beads, and any two beads within a prescribed cutoff distance  $r_c$  are connected with each other through a spring. The formed bead-spring network has zero potential energy at the native conformation. The energy incurred by conformation change is then the sum of spring harmonic potential (see Methods). We collect the first 20 mode fluctuations (mode shapes) obtained from the eigenanalysis of the potential Hessian matrix and compute the cross-correlations between all residue pairs (Fig. 1d). The cross-correlations underscore the residue pairs that have a high degree of synergy across 20 mode fluctuations. The pairs that mostly move toward the same direction have high correlation, while that mostly move toward the opposite directions have high anticorrelation. For each protein, we calculate the correlation map by taking the trace of the cross-correlation matrix and normalizing along diagonal components. The correlation map thus identifies the residue pairs that are important for the collective dynamics of protein accessible at the native conformation.

To encode structural and dynamic information into the protein graph representation, we merge the contact map and correlation map into a single adjacency matrix. The residue pairs in contact are first connected together with *contact edges*. Aside from the residue pairs with contact edges, other residue pairs with absolute correlation values no less than 0.5 ( $\bar{c}_{ij} \geq 0.5$ ) are connected with *correlation edges*. Each node is assigned with a one-hot feature vector of 21 dimensions according to the type of amino acid it holds. The constructed protein graphs therefore encompass sequential, structural, and dynamic information of proteins in an unified representation.

## **Correlation edges representing the dynamic features of proteins facilitate message propagation between residues in GNN**

To explore the dynamic features obtained from NMA, we examine the individual and cumulative fractions of the first 20 modes of several PDB chains, covering different molecular functions and residue numbers (Fig. 2a). The result shows that the individual contributions from modes decrease drastically as the mode number increases. For the first 20 modes, in these examples, all of the cumulative fractions account for more than 50% of all available modes. The high-frequency modes are relatively negligible compared with low-frequency modes in terms of the global dynamic behavior of proteins. Our method includes modes from low to high frequencies and therefore incorporates the most prominent fluctuations in global protein dynamics.

The upper panel of Fig. 2b shows the comprehensive frequency distributions of the first 20 modes in our dataset. The average frequencies linearly increase with mode number from 0.075 to 0.331, and the standard deviations increase from 0.040 to 0.118. By truncating the first 20 modes from NMA, a wide range of modal frequencies and fluctuations are extracted and encoded into the correlation maps. Of the five largest populations of MF-GO annotations, including metal ion binding (GO:0046872), protein binding (GO:0005515), hydrolase activity (GO:0016787), oxidoreductase activity (GO:0016491), and aspartic-type endopeptidase activity (GO:0004190), universal frequency increments with respect to mode number are observed, as shown in the bottom panel of Fig. 2b. Although the modal frequencies of these functional annotations overlap, these functions have different frequency averages and deviations. It is possible that the multifunctional nature of proteins gives rise to large frequency overlaps for different functional annotations.

Through our graph construction framework, a considerable number of correlation edges are added to the protein graphs, as shown in Fig. 2c. Although a large number of the PDB entries have few correlation edges, the number of correlation edges in some PDB entries can be nearly eightfold the number of contact edges. Our work has benefited from these correlation edges, which fundamentally change the way GNNs draw inferences and reason down to the residue level. Fig. 2d shows the distributions of contact and correlation edges with respect to ten MF-GO terms in our dataset. Note that the number of correlation edges for aspartic-type endopeptidase activity (GO:0004190) is markedly smaller than those of the other terms.

Moreover, zinc ion binding (GO:0008270) has few PDB entries with extremely large numbers of correlation edges (approximately over 120,000). These correlation edges alter protein graph representations and increase the amount of dynamic information encoded into the graphs. The distributions of contact edges are similar across different terms, but those of correlation edges are remarkably dissimilar from each other, indicating that the dynamic information encoded in correlation edges plays an important role in MF-GO terms and that our graph representations contain more information, better representing and differentiating proteins in high-dimensional space.

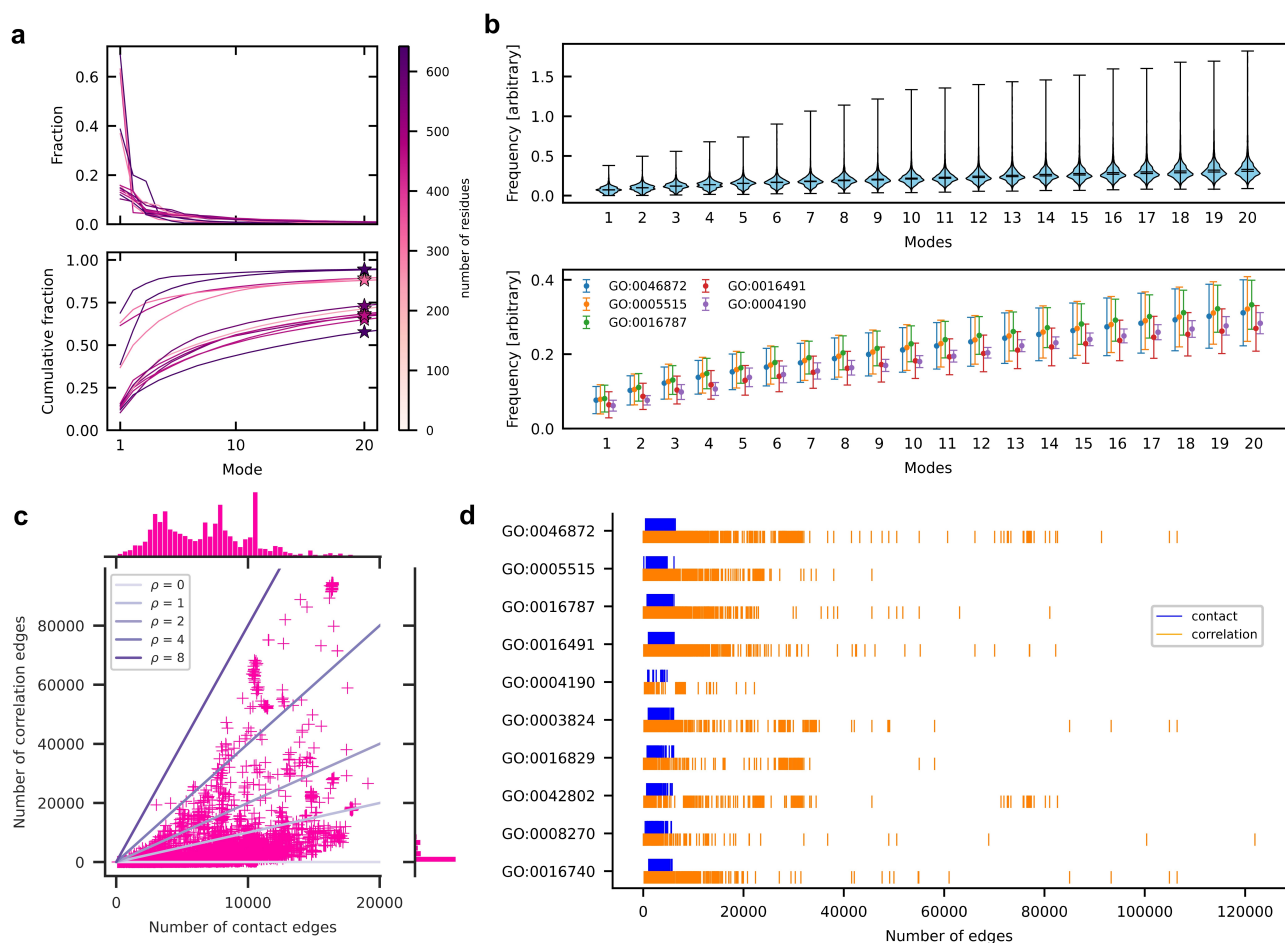


**Fig. 2 Summary of the modal frequencies and correlation edges of proteins.** **a** Individual and cumulative fractions of the first 20 modes compared to the complete set of modes. The number of residues are colored accordingly. Example PDB entries include PDB 1SY1, 1SY2, 2OY4, 2RJQ, 3TL9, 3TYI, 3ZFZ, 3ZR0, 4AUO, 5D8V, 5GHI, 5GHI, and 7C8D. **b** Modal frequencies of PDB entries in the dataset. The upper panel shows the distribution of all PDB entries. The bottom panel shows the mean and standard deviation values with respect to the five largest populations of MF-GO annotations. **c** Number of contact and correlation edges in the dataset.  $\rho$  denotes the number ratio of correlation edges to contact edges. **d** Number of contact and correlation edges for the ten largest populations of MF-GO annotations.

## Dynamics-informed representation increases the discriminatory power for function classification

The correlation edges in our graph construction establish connections between residues far apart in space but dynamically correlated in terms of functional motions. These distant connections ameliorate the information flow in graphs by permitting message to pass over a long distance without the limitation imposed by the depth of graph convolutional layers. This largely alleviates the restriction of the depth of GNNs in consideration of the computing efficiency. To examine the effectiveness of correlation edges for protein function classification, we construct two sets of graphs, one with only contact edges and another with both contact and correlation edges (Fig. 3a). In addition to graphs, we calculate 1D and 2D persistence diagrams of  $C^\alpha$  atoms in each protein, the coarsened topological features measured by persistent homology<sup>20,28</sup>, and embed the diagrams into persistence images via Gaussian kernels and pixelated integrals<sup>29</sup> (see Methods). Our model takes input from three feature pipelines: (1) spatial information from the contact map where residue pairs are closer than cutoff distance  $r_c$  such as 8Å and 12Å, (2) topological information from the persistence image, which is preprocessed as vectors of 625 dimensions, and (3) dynamic information based on the correlation map such that residue pairs with absolute correlation no less than 0.5 are connected with correlation edges if they are not in contact. As shown in Fig. 3b, the graphs are fed into five graph convolutional layers in sequence. Each layer of graph convolution takes the adjacency matrix and node features as input and outputs the aggregated node features to the next layer. In this work, we adopt the graph convolutional network (GCN) by Kipf *et al.*<sup>30</sup> and Graph SAMple and aggreGatE (GraphSAGE) by Hamilton *et al.*<sup>31</sup>. Global maximum pooling (GMP) is applied to readout from five graph convolutional layers the residues that are functionally important and prominent in their nearest to fifth nearest neighbors. Linear layer and rectified linear unit (ReLU) activation are used to embed persistence image and graph pooling layer into vector representations of 512 dimensions. The persistence representation and the graph representation are then concatenated and passed into a fully connected layer with sigmoid activation. The final outputs are the probabilities of the certain protein of interest pertaining to the particular GO annotations (see Methods).

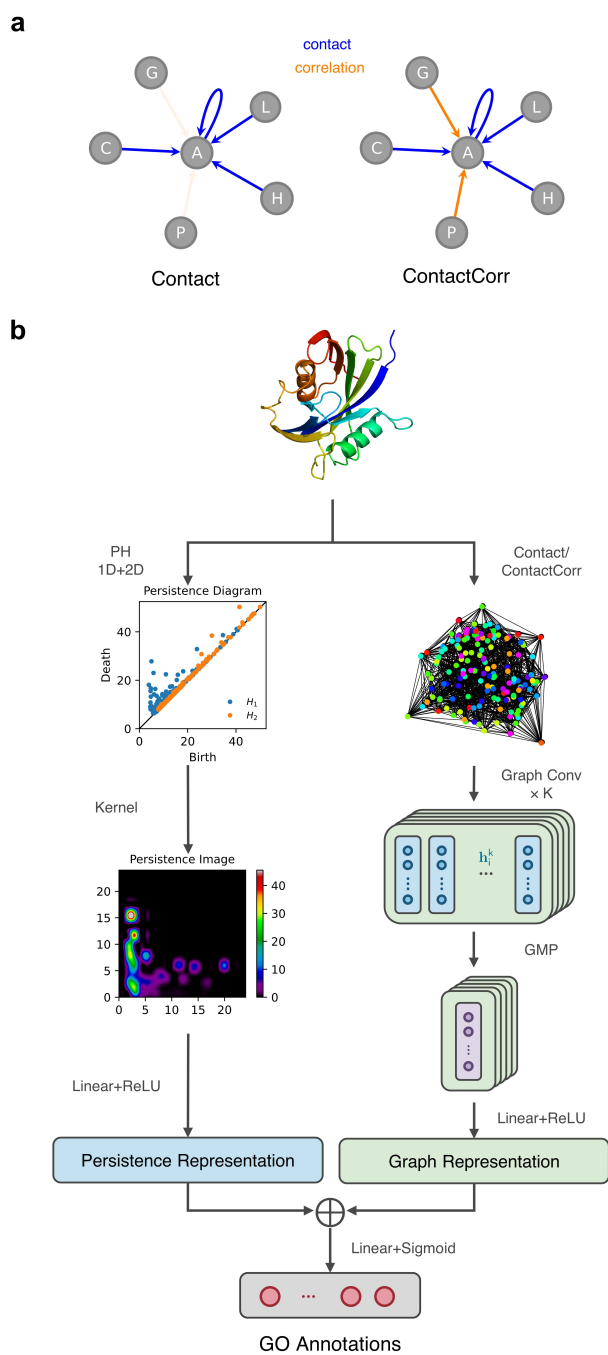


**Fig. 3 ProDAR model architecture.** **a** Graph with only contact edges (Contact) and graph with both contact and correlation edges (ContactCorr). **b** Three data pipelines of spatial (contact map), topological (persistence diagram), and dynamic (correlation map) features for learning protein functions. Five graph convolutional layers ( $K = 5$ ) and GMP are used to extract the functionally important residues. 1D and 2D persistence diagrams ( $H_1, H_2$ ) are transformed into a persistence image via Gaussian kernels and pixelated integrals. The embedded persistence and graph representations are concatenated into protein representations.

To examine the utility and importance of structural, topological, and dynamic features in predicting protein functions, we design four model architectures: Contact, ContactPers, ContactCorr, and ContactCorrPers, with each model having different combinations of feature pipelines (Table 1). We also construct two datasets with different cutoff distances  $r_c = 8\text{\AA}$  and  $r_c = 12\text{\AA}$  to observe the effect of the cutoff on the classification performance. The choices of cutoff distance for graph-based protein feature extraction vary from approximately 6 to 15 Å in the literature<sup>17,20,32</sup>. Here we follow the cutoff 8 Å used by PersGNN<sup>20</sup> for a fair comparison. Furthermore, to avoid the influence of imbalanced positive and negative samples, we calculate the balanced accuracy (arithmetic mean of the true positive rate and true negative rate) of the test set as the immediate metric of model performance. Due to the usage of weighted binary cross-entropy loss (Methods), the models tend to have higher final recall at the cost of precision. We regard this phenomenon as the desired outcome because we expect models to capture as many functions as possible.

**Table 1 Four model architectures with different combinations of feature pipelines.**

Model	Feature Pipelines		
	Contact map	Correlation map	Persistence diagram
Contact	•		
ContactPers	•		•
ContactCorr	•	•	
ContactCorrPers	•	•	•

Table 2 presents the classification performance of all models in comparison with that of DeepFRI<sup>17</sup> and PersGNN<sup>20</sup>. We evaluate the trained classifiers by leveraging the threshold at the final sigmoid activation. The area under the precision-recall curve (AUPR) and the maximum F1 score (F1-max) are calculated to compare the model performance. We find that GCNs in general outperform GraphSAGEs with maximum aggregators, despite a small margin of improvement. This agrees with the previous experimental and theoretical study showing that the mean aggregator essentially retains more discriminatory power than max aggregators since mean aggregator, although more simplistic than the sum aggregator, learns the distribution of the node features such that it can be as powerful as the sum aggregator if the feature distribution is diverse or the recovery to the sum is possible<sup>33</sup>. Our result also shows that ContactPers and ContactCorr comparably enhance the representational capacity of the Contact model, with the ContactCorr model outperforming ContactPers by up to 0.005 in AUPR and 0.004 in F1-max score

when GraphSAGE and the  $r_c = 12\text{\AA}$  dataset are used. However, it is worth noting that by combining persistence and correlation together, the ContactCorrPers model has a notable performance gain that is greater than the direct sum of individual improvements by ContactPers and ContactCorr. The most robust classifier of the above models is ContactCorrPers with GCN convolutional layers for both the 8  $\text{\AA}$  and 12  $\text{\AA}$  datasets. This model outperforms the state-of-the-art models in terms of AUPR and F1-max scores by significant margins, as presented in Fig. 4 and Table 2. Fig. 4c illustrates two-dimensional projections (t-distributed stochastic neighbor embedding (t-SNE)) of final protein representation vectors by the ContactCorr network. The Kullback–Leibler divergences (KL-divergences) of the two projections by the Contact and ContactCorr networks are 1.267 and 1.145, respectively, supporting that the ContactCorr network can better separate proteins in high dimensional space. Dynamics-informed protein representation can thus increase the discriminatory capacity of neural networks for protein function prediction.

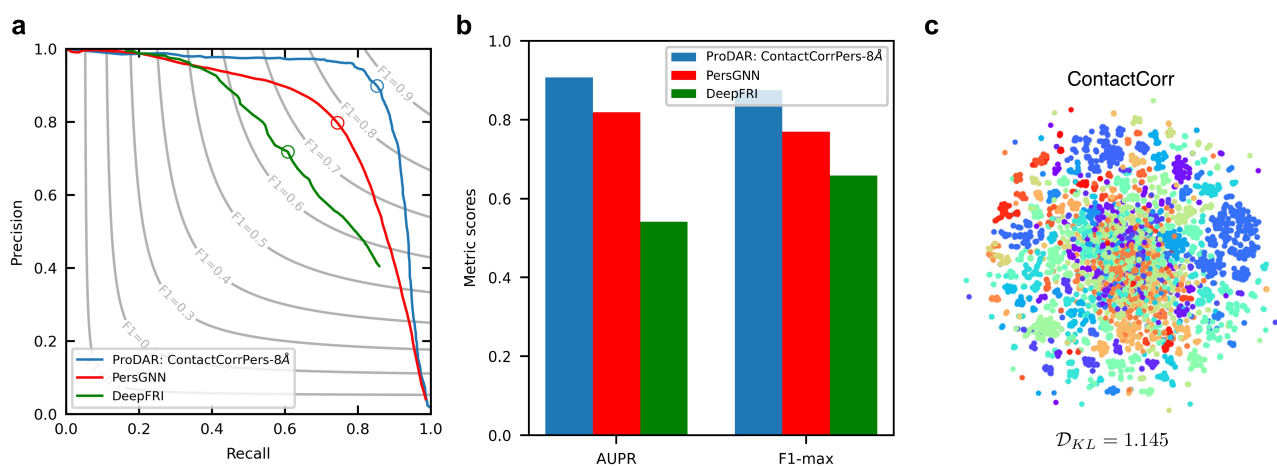


**Fig. 4 Classification performance of ProDAR on MF-GO annotations.** **a** Precision and recall curve of ProDAR, PersGNN, and DeepFRI. **b** AUPR and F1-max score of ProDAR, PersGNN, and DeepFRI. **c** Two-dimensional t-distributed stochastic neighbor embeddings (t-SNE) of protein representations predicted by ContactCorr network. Each point represent a protein, whose color denotes the primary function predicted with the highest probability. 24,755 training PDBs and 4,126 testing PDBs are used by PersGNN. 29,902 training PDBs and 3,416 testing PDBs are used by DeepFRI.

## DARs are critical functional residues with dynamic importance

Proteins are complex molecular machines whose functions are closely correlated to key functional residues. The experimental approaches usually include indirect methods, *e.g.* ,point mutation of specific residues, to identify the important collections of residues and their underlying functional mechanism.

**Table 2 Performance comparison with other models.** Our best-performing models are highlighted with boldface. †24,755 training PDBs and 4126 testing PDBs from Arabidopsis, Celegans, E.coli, Fly, Human, Mouse, Yeast, and Zebrafish species. ‡29,902 training PDBs and 3,416 testing PDBs mainly from Eukaryote, bacteria and viruses, evaluated under 10 bootstrap iterations.

$r_c$	Model	AUPR	F1-max
8 Å	Contact (GCN)	0.898	0.863
	ContactPers (GCN)	0.904	0.868
	ContactCorr (GCN)	0.902	0.867
	ContactCorrPers (GCN)	<b>0.907</b>	<b>0.875</b>
	Contact (GraphSAGE)	0.876	0.826
	ContactPers (GraphSAGE)	0.896	0.861
	ContactCorr (GraphSAGE)	0.898	0.861
	ContactCorrPers (GraphSAGE)	0.904	0.871
	PersGNN†	0.820	0.770
	10 Å	DeepFRI‡	0.430
12 Å	Contact (GCN)	0.904	0.879
	ContactPers (GCN)	0.910	0.878
	ContactCorr (GCN)	0.910	0.879
	ContactCorrPers (GCN)	<b>0.916</b>	<b>0.895</b>
	Contact (GraphSAGE)	0.900	0.871
	ContactPers (GraphSAGE)	0.905	0.873
	ContactCorr (GraphSAGE)	0.910	0.877
	ContactCorrPers (GraphSAGE)	0.915	0.885

Examples abound in active sites of an enzyme, ligand-binding sites, ionic gating, protein-protein interaction (PPI), and mechanical conformation changes involving soft and stiff secondary structures<sup>17</sup>. Many deep learning models have been applied to identify the functional residues in proteins<sup>34,35</sup>. The class activation map (CAM) has been widely applied in the field of computer vision to provide a visual explanation of convolutional neural networks<sup>36</sup>. Our work has benefited from Grad-CAM<sup>17,27</sup>, which takes the derivatives of network outputs with respect to feature maps. The method either sums or averages the derivatives in spatial dimensions. The localized importance is then achieved by the sum of the feature maps weighted by the obtained derivatives (gradients). Unlike the original Grad-CAM averaging the derivatives via spatial pooling, in this work, we keep the vector form of derivatives and take the residewise inner product of derivatives with residue-level embeddings across all graph convolutional layers (see Methods). This allows us to obtain residue-level activation for functional site identification while ensuring independence between two feature vectors. The importance weight of the feature map at channel  $i$  for function  $m$  ( $\alpha_i^m$ )

can thus be expressed as

$$\alpha_i^m = \sum_{l=1}^{d_G} \sum_{k=1}^K \sum_{j=1}^{d_N} w_l^m w_{(k-1)d_N+j}^l \mathbf{1} \left( \max_s \{h_{sj}^k\} = h_{ij}^k \right) \quad (1)$$

where  $w_{(k-1)d_N+j}^l$  is the equivalent linear weight from the GMP layer to the graph embedding  $l$ , and  $w_l^m$  is the equivalent linear weight from graph embedding to the output layer (see the red blocks in Fig. 5a).  $d_N$  and  $d_G$  are node and graph embedding dimensions, respectively.  $K$  is the total depth of graph convolutions.  $\mathbf{1}$  is the binary indicator function which equals 1 if the true condition is satisfied. For each PDB chain, we record the outputs activated by five graph convolutional layers (red arrow in Fig. 5a) and calculate the sum of the outputs weighted by the partial derivatives of GO annotations with respect to the feature channels in the convolutional layers. As the outputs forwardly propagate through two fully connected layers with layer normalization and ReLU activation, the corresponding weights are retrieved during calculations.

Fig. 5b shows the Grad-CAMs of hMTH1 (PDB 5GHI) predicted by the Contact and ContactCorr network with a cutoff of 12Å. Both activation maps successfully identify hydrogen bonding aspartate residues (Asp119 and Asp120), while only the ContactCorr network activates L-A, the loop surrounding the binding pocket (Fig. 5c-d). As shown in Fig. 5b,e, the difference in the saliency maps ( $\Delta$ SALS, see Methods) emphasizes residues from Phe113 to Asp120 and loop L-A, reflecting the dynamic significance of their roles in substrate binding<sup>14</sup>. The binding pocket changes conformation to recognize different substrates, as shown previously in Fig. 1b<sup>14</sup>. Notably, the peaks of the activation map by the ContactCorr network are generally larger than those by the Contact network. This is attributed to the contribution of the correlation edges in the ContactCorr network. The correlation edges reinforce the activation of residues and provide more confident functional inferences in graphs. These results show that with dynamic information in graph representation, ProDAR is able to identify the residues that are overlooked by the networks with mere input from the contact map.

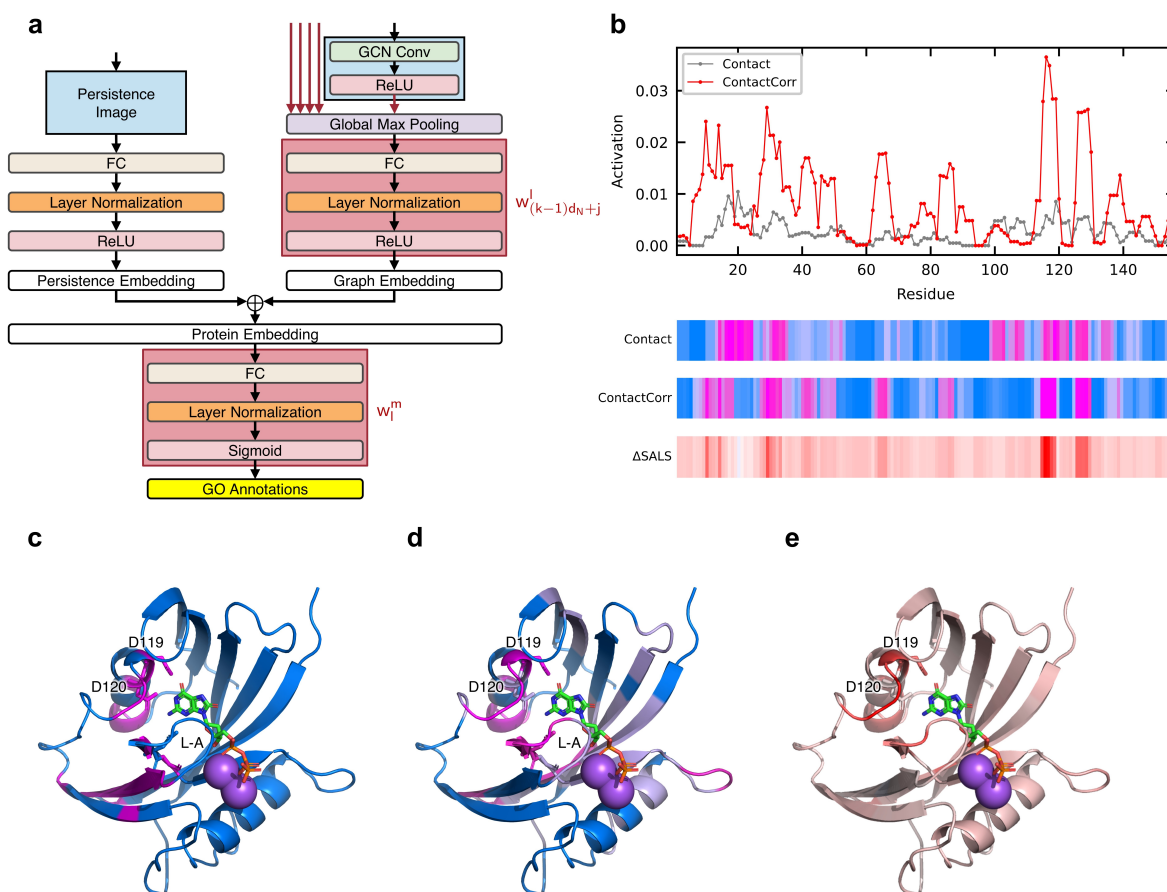


**Fig. 5 DARs and functional residue identification.** **a** Schematic derivation of the importance weight  $\alpha_i^m$  at channel  $i$  of the node embeddings for function  $m$ . **b** Grad-CAMs of the Contact and ContactCorr networks for PDB 4GHI and the saliency difference ( $\Delta$ SALS) between the Grad-CAM obtained by the ContactCorr network and the Grad-CAM obtained by the Contact network. **c-d** PDB structure annotations of activation maps predicted by **c** Contact and **d** ContactCorr networks. All residues are colored with a marine-magenta gradient according to the Grad-CAM profiles after min-max normalization, with more salient residues highlighted in magenta and less salient residues colored in marine blue. **e** PDB structure annotation of the saliency difference. All residues are colored with blue-white-red gradient. The residues colored in red and blue represent reinforcement and suppression, respectively, while the residues colored in white are comparably salient in both Grad-CAMs.

## ProDAR provides molecular insights into point mutations in proteins

Fig. 6 demonstrates the Grad-CAMs of nitrophorin 4 (NP4)<sup>37</sup>, a ferric heme protein that transports nitric oxide (NO) from blood-sucking insects to victims. The MF-GO terms of nitrophorin include oxidoreductase activity, metal ion binding, histamine binding, and nitric oxide binding. The A-B loop (residues 31-37) and G-H loop (residues 125-133) are indicated to be responsible for the pH dependence of NO release<sup>37</sup>. In the absence of NO at high pH, the distal pocket in wild-type NP4 is open with poorly ordered A-B and G-H loops far from the heme. When NO binds to wild-type NP4 at low pH, the distal pocket collapses into a closed conformation, and the 130-131 peptide bond flips and forms a buried hydrogen bond between the Asp30 side chain and Leu130 carbonyl oxygen. Fig. 6a shows the activated residues of NP4 with a point mutant T121V (PDB 1SY1). Both the A-B and G-H loops are activated in the Grad-CAM predicted by the ContactCorr network, while only the A-B loop is activated by the Contact network. Surprisingly, despite the absence of heme and NO during both the training and inference phases, the ContactCorr network can still successfully identify Leu130, which moves into the distal pocket and contacts NO in the T121V structure.  $\Delta$ SALS further indicates that residues 30-34, 39-43, 120-124, and 129-130 are more salient in the ContactCorr activation. This agrees with the corresponding functional sites in NP4 in that residues 30-34 and 129-130 are inside A-B and G-H loops, respectively, and that residues 39-43 are located at the  $\beta$ -sheet in connection with the A-B loop. Moreover, residues 120-124 are pertinent to hydrogen bonds with water in the distal pocket<sup>37</sup>. In contrast, the residues near Val25 and Tyr105, the  $\beta$ -sheets with commonplace structural motifs, are suppressed. This implies that the ContactCorr network, unlike the Contact network, has a stronger denoising capability and does not activate trivial residues in protein.

In the structure of the D129A/L130A mutant of NP4, the 129-130 peptide bond is shifted by  $\approx 2$  Å, and Ala130 is rotated away from the heme, leading to an enlarged distal pocket for additional water molecules. This nullification of abilities for NO binding and release is precisely reflected in the activation map by the ContactCorr network. By comparing the Grad-CAMs of the ContactCorr network in Fig. 6a and b, we note that Asp30, Ala129, and Ala130 are deactivated in the D129A/L130A structure. Moreover, the Grad-CAMs of the ContactCorr network are relatively more stable in the T121V and D129A/L130A structures. The two activation profiles exhibit similar activated sites. However, despite the ability to consistently

identify some parts of functional residues (such as residues around 40 and 121), the Grad-CAMs of the Contact network show incoherent activation profiles for the other residues. In particular, it is unable to properly respond to the D129A/L130A mutations, leading to erroneous overactivation around Asp147 and Tyr134. Additionally, note that N-terminus, which forms hydrogen bonds with Asp 129 in the T121V structure and with Ala130 in the D129A/L130A structure, has larger activation values in the ContactCorr profiles than those in Contact profiles. This reveals that ProDAR has better sensitivity to structural nuance and stronger confidence for functional residue identification.

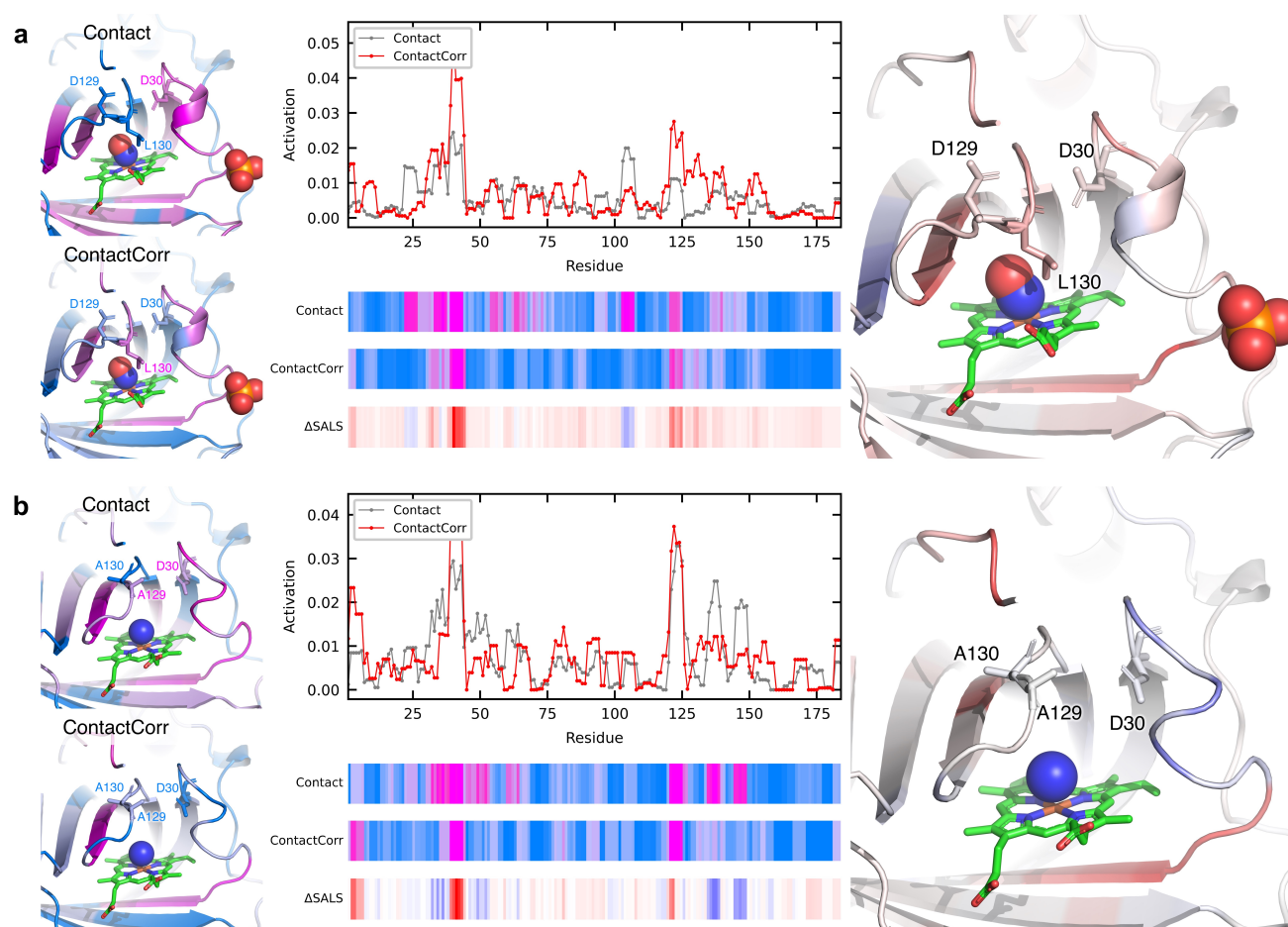


**Fig. 6 Robustness and expressiveness of ProDAR to reflect point mutations in protein.** **a** Grad-CAMs and  $\Delta$ SALS on T121V mutant of nitrophorin 4 (NP4) with nitric oxide, ferric heme, and phosphate ion (PDB 1SY1). **b** Grad-CAMs and  $\Delta$ SALS on D129A/L130A mutant of NP4 with ferric heme and ammonium ion (PDB 1SY2). In Grad-CAMs, all residues are colored with marine-magenta gradient according to the Grad-CAM profiles after min-max normalization, with more salient residues highlighted in magenta and less salient residues colored in marine blue. In  $\Delta$ SALS, all residues are colored with blue-white-red gradient. The residues colored in red and blue represent reinforcement and suppression, respectively, while the residues colored in white are comparably salient in both Grad-CAMs.

## Residue-level activation of ProDAR on the SARS-CoV-2 RBD

At the forefront for the fight against the highly pathogenic severe acute respiratory syndrome coronavirus-2 (SARS-CoV-2), identifying residues of dynamic importance is urgently needed for structure-based vaccine design<sup>38,39</sup>. Here, we apply ProDAR to the structure of the SARS-CoV-2 receptor binding domain (RBD) to determine whether our model is able to identify the important residues in the unseen and fragmented structure. Fig. 7a shows the complex of the SARS-CoV-2 RBD and cell receptor angiotensin converting enzyme 2 (ACE2) in cats<sup>40</sup>. Previous cryo-EM studies of the SARS-CoV spike protein and its interaction with ACE2 have shown that ACE2 receptor binding is a critical step for SARS-CoV to enter target cells<sup>41</sup>. However, the interaction between the SARS-CoV-2 RBD and ACE2 at the atomic level is not well understood. At the hydrophilic interface between the SARS-CoV-2 RBD and human ACE2 (hACE2), 13 hydrogen bonds and 2 salt bridges have been found previously<sup>39</sup>. Similar interactions have been found at the interface between the SARS-CoV-2 RBD and cat ACE2 (cACE2)<sup>40</sup>. In the complex of SARS-CoV-2 RBD and cACE2<sup>40</sup> (Fig. 7a), seven residues (Leu455, Phe456, Tyr473, Ser477, Phe486, Asn487, and Tyr489) on the  $\beta 1'/\beta 2'$  loop of SARS-CoV-2 RBD have been found in contact with cACE2, including 2 hydrogen bonds (Ser477 with Gln18 of cACE2 and Asn487 with Tyr83 of cACE2<sup>40</sup>). As shown in Fig. 7b and c, ProDAR successfully activates the aforementioned residues in the Grad-CAM of the ContactCorr network. Thr500, Asn501, and Tyr505, the residues contributing to the contacts of SARS-CoV-2 RBD with both hACE2 and cACE2<sup>40</sup>, are also activated. Although neither the complex nor the individual atomic structure of SARS-CoV-2 RBD and cACE2 is in the training dataset and cACE2 is not present in the inference phase, the model yet exhibits strong predictive power and makes cogent inference on residues.

In the Grad-CAM of the ContactCorr network, we find that there is a second largest peak around Ser373, which is not widely discussed in the literature. Molecular dynamics (MD) simulation is performed to confirm whether the residues around Ser373 are indeed crucial for protein functions. We simulate the full atomistic model of SARS-CoV-2 spike glycoprotein and find that Ser373 forms hydrogen bonds with other SARS-CoV-2 RBDs in the trimeric unit. In Fig. 7d, we show the hydrogen-bonding patterns between the SARS-CoV-2 RBDs in the entire homotrimeric spike glycoprotein<sup>38</sup>. Our results indicate that in the closed state, Ser373 tends to form hydrogen bonds with Asp405, Glu406, and Arg408 and

stabilize the trimer of RBDs. At 0.77 ns, two and one hydrogen bonds form at the A-B and B-C interfaces, respectively, while no hydrogen bonds are found at the C-A interface. Fig. 7e shows the number of hydrogen bonds between SARS-CoV-2 RBDs. Three Ser373–Asp405 hydrogen bonds form at the same time, while Arg408–Ser373 pairs can form at most one hydrogen bond simultaneously. The occupancy analysis also shows that S373:OG-D406:OE1 is the most stable hydrogen bond, with occupancy close to 80%, and that S373:OG-D405:OD1 and R408:NH2-S373:O have occupancy values of approximately 60%, whereas S373:OG-D405:CG has only 13.86% occupancy (Fig. 7h). The results again reveal that ProDAR can pinpoint the critical residues that have important functionality and molecular characteristics, even though the structure is not included in the training dataset.

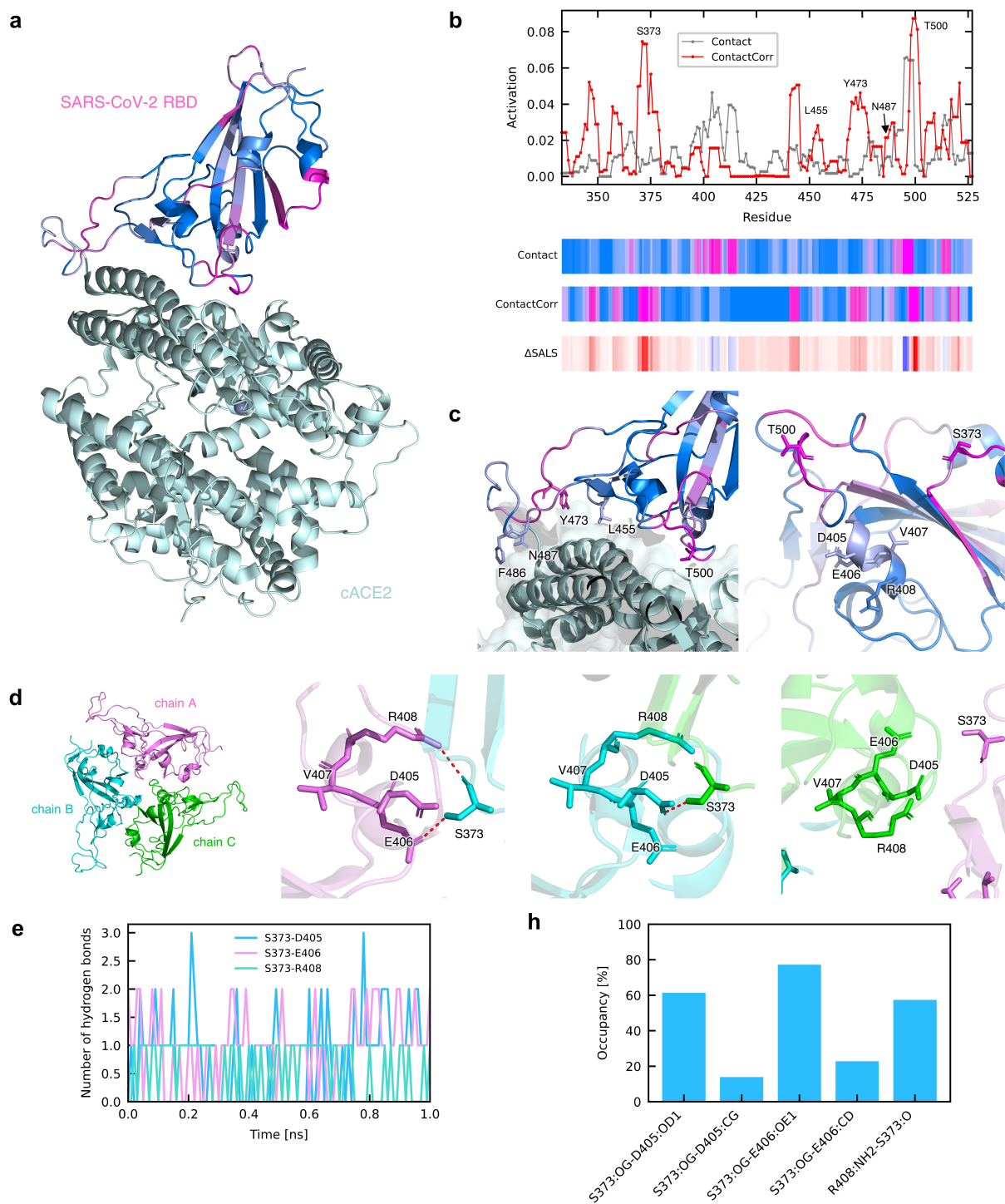


**Fig. 7 DARs and hydrogen-bonding interactions in SARS-CoV-2 receptor-binding domain (RBD)** **a** Grad-CAM and  $\Delta$ SALS of SARS-CoV-2 RBD (PDB 7C8D). **b** Residue activation predicted by ContactCorr network on SARS-CoV-2 RBD structure. **c** Complex structure of cat angiotensin converting enzyme 2 (cACE2) bound to SARS-CoV-2 RBD. **d** Trimeric unit of SARS-CoV-2 spike glycoprotein (PDB 6VXX). Only SARS-CoV-2 RBD regions are visualized. The three panels on the right are hydrogen-bonding poses between A and B chains, B and C chains, and C and A chains, respectively. **e** Number of hydrogen bonds between SARS-CoV-2 RBDs over 1 ns MD simulation in the homotrimeric spike glycoprotein. Three donor-receptor pairs are counted simultaneously. **h** Hydrogen bond occupancy of each donor-receptor pair.

## Discussion

Through MD simulations, different conformations occurring at the nanosecond scale can be observed that, for instance, allow ion passing through the selectivity filters or encourage alternating conformations of transmembrane helices. On the other hand, principal component analysis (PCA) has also been increasingly used to extract the collective motions of macromolecules, whose thermal fluctuations conceal underlying contributions from highly cooperative movements that are closely related to their biological functions<sup>13</sup>. NMA, a subgenre of PCA that provides a harmonic approximation of the energy landscape, has been beneficial for this work and has enabled fast screening over an astronomical number of conformations for proteins.

Although the correlation map derives from and combines modal frequencies and fluctuations in a single representation, it is possible to separately encode them. The modal frequencies can be separated as a feature vector for model input. Additionally, the mode fluctuations are a large set of vectors that can be manipulated by various mappings and operations. The correlation map is one possible pairwise reduction from the complete cross-correlation matrix. Other reduction approaches, such as the tensor invariant, infinity norm, and single value decomposition methods, can be employed. Helmholtz decomposition can also be used to compute the irrotational and solenoidal parts of mode fluctuations such that some rotational modes with significant physical meanings but modest inner product values can be successfully extracted.

There are other available encoding methods from bioinformatics and deep learning, including the principal component score Vectors of Hydrophobic, Steric, and Electronic properties 8 (VHSE8)<sup>42</sup>, blocks amino acid substitution matrices (BLOSUM62)<sup>43</sup>, and long short-term memory (LSTM)-based methods<sup>44,45</sup>. This work nonetheless focuses on augmented functional residue identification and the enhanced classification performance of our model. Other embedding methods of amino acids are temporarily out of the scope of this work but are indeed worthy of further experimentation for advanced inference problems, such as mutation detection and functional residue segmentation.

Different approaches for encoding dynamic information into graphs are of interest in future studies. The straightforward merging of contact and correlation edges can be replaced by more sophisticated graph architectures, *e.g.*, dual graphs, directed graphs, and graphs with multiple types of edges. The values obtained from the correlation map can also be applied as the weights for edges, resembling the motifs

of attention-based networks (for example, Graph Attention network). While this work focuses on the utility of correlation edges and their implications for functional residue identification, we demonstrate that ProDAR has remarkable robustness against noise and has unprecedented interpretability for both regular and mutated PDB structures. Our model also shows strong generalizability to unseen PDB structures. Without *a priori* knowledge of ligands and hydrogen bonds, ProDAR can still provide reliable inferences regarding PDB structures at the residue level.

## Conclusion

Herein, we describe a method to encode the dynamic information of proteins in graph representation. This work is the first to incorporate the NMA of proteins into a deep learning framework for functional prediction. In addition to the contact map commonly used by the previous graph-based deep learning models<sup>17,19,20</sup>, we compute the correlation map and add edges between the residue pairs that are highly correlated in the first 20 modes. These correlation edges connect the dynamically correlated residues distant in space and allow message to pass over long spatial distances. The model therefore alters the graph inference regime and better captures the dynamic information intrinsically residing in the native conformation of proteins. Such dynamics-informed graph representation achieves supreme performance in protein function classification and increases the discriminatory power of neural networks. The models with input from dynamic information identify DARs that are both structurally and functionally meaningful to protein function.

To summarize, we close the information gap between structure and function by introducing dynamic analysis in the graph construction process. Our method bridging structure and function with dynamics provides the missing part of the deep learning framework for protein function prediction and sketches a comprehensive picture from sequence to function, with great potential to advance science in mutation detection and function engineering through rapid screening over large sequential and structural spaces.

# Methods

## Normal mode analysis (NMA)

Given a surrogate physical system for a protein represented by  $N$  interaction particles ( $C^\alpha$  atoms), the potential energy can be expressed as the Taylor expansions near the native conformation  $\mathbf{q}^o$ . By omitting higher order term to the second order, the required energy to transit from  $\mathbf{q}^o$  to  $\mathbf{q}$  becomes the sum of the pairwise potentials

$$\begin{aligned} V(\mathbf{q}) - V(\mathbf{q}^o) &= \sum_{i=1}^{3N} \sum_{j=1}^{3N} \left. \frac{\partial^2 V}{\partial q_i \partial q_j} \right|_{\mathbf{q}^o} (q_i - q_i^o)(q_j - q_j^o) \\ &= \sum_{i=1}^{3N} \sum_{j=1}^{3N} H_{ij} (q_i - q_i^o)(q_j - q_j^o) = \frac{1}{2} \Delta \mathbf{q}^\top \mathbf{H} \Delta \mathbf{q} \end{aligned} \quad (2)$$

where  $\mathbf{H}$  is the  $3N \times 3N$  Hessian matrix of the second derivatives of the potential with respect to particle coordinates at equilibrium

$$H_{ij} = \left. \frac{\partial^2 V}{\partial q_i \partial q_j} \right|_{\mathbf{q}^o} \quad (3)$$

. By considering only the internal interactions under classical regime, the equation of motion of particles can be written as

$$\mathbf{M} \Delta \ddot{\mathbf{q}} + \mathbf{H} \Delta \mathbf{q} = \mathbf{0} \quad (4)$$

where  $\mathbf{M}$  is the diagonal matrix of particle masses. The solution to equation (4) is a  $3N$ -dimensional harmonic oscillator, which can be further generalized as

$$\Delta \mathbf{q}^{(k)} = \mathbf{u}^{(k)} = \mathbf{a}^{(k)} \exp(-i\omega_k t) \quad (5)$$

where  $\mathbf{a}^{(k)}$  is a complex vector containing the amplitude and phase factor, and  $\omega_k$  is the frequency of the  $k$ -th solution. Substituting the solution (equation (5)) into equation (4) gives the generalized eigenvalue equation

$$\mathbf{H} \mathbf{u}^{(k)} = \omega_k^2 \mathbf{M} \mathbf{u}^{(k)} \quad (6)$$

. By stacking a complete set of solution vectors into a single matrix  $\mathbf{U}$  and arranging the corresponding squared frequencies as a diagonal matrix  $\Lambda$ , the equation (5) can be rewritten as

$$\mathbf{H}\mathbf{U} = \mathbf{M}\mathbf{U}\Lambda \quad (7)$$

. The equation (7) can be solved by transforming it into a standard eigenvalue equation through mass-weighted transformations:

$$\tilde{\mathbf{U}} = \mathbf{M}^{\frac{1}{2}}\mathbf{U} \quad (8)$$

$$\tilde{\mathbf{H}} = \mathbf{M}^{-\frac{1}{2}}\mathbf{H}\mathbf{M}^{-\frac{1}{2}} \quad (9)$$

. Thus the massed-weighted eigenvalue equation becomes

$$\tilde{\mathbf{H}}\tilde{\mathbf{U}} = \tilde{\mathbf{U}}\Lambda \quad (10)$$

. The equation (10) has  $3N - 6$  non-zero eigenvalues, reflecting six degenerate eigenstates of three translational and three rotational degrees of freedom. The mass-weighted Hessian  $\tilde{\mathbf{H}}$  remains real, symmetric, and positive semi-definite as the original Hessian  $\mathbf{H}$  by construction. Its eigenvectors  $\tilde{\mathbf{u}}^{(k)}$  (column vectors of  $\tilde{\mathbf{U}}$ ,  $k = 1, 2, \dots, 3N$ ) form an orthonormal basis and construct normal modes of the system in the mass-weighted coordinates. The original normal modes in Cartesian coordinates can hence be obtained by  $\mathbf{U} = \mathbf{M}^{-\frac{1}{2}}\tilde{\mathbf{U}}$ . Since  $\tilde{\mathbf{U}}$  is a unitary matrix, the orthogonality is again satisfied by

$$\mathbf{I} = \tilde{\mathbf{U}}^{\top}\tilde{\mathbf{U}} = \mathbf{U}^{\top}\left(\mathbf{M}^{\frac{1}{2}}\right)^{\top}\mathbf{M}^{\frac{1}{2}}\mathbf{U} = \mathbf{U}^{\top}\mathbf{M}\mathbf{U} \quad (11)$$

The energy change associated with a given mode  $k$  is proportional to the square of its mode frequency  $\omega_k$ , as seen in equation (2):

$$V\left(\mathbf{u}^{(k)} = \Delta\mathbf{q}^{(k)}\right) = \frac{1}{2}\left(\mathbf{u}^{(k)}\right)^{\top}\mathbf{H}\mathbf{u}^{(k)} = \frac{\omega_k^2}{2} \quad (12)$$

Fluctuations along the high-frequency modes are therefore energetically more expensive than those along

the low-frequency modes. According to the equipartition theorem, the vibrational energy is prone to be equally partitioned among all the modes, such that the vibrational amplitudes are scaled by  $1/\omega_k^2$ .

NMA is based on the assumption of symmetric and positive semi-definite Hessian matrix. Strictly speaking, energy minimization needs to be carried out before performing NMA on protein crystal structure to ensure the local energy minimum. However, energy minimization is computationally intensive. An alternative method is adopting elastic network model (ENM) that accept the initial structure (crystal structure from PDB) to be the conformation at local energy minimum.

## Anisotropic network model (ANM)

Anisotropic network model (ANM) is the most broadly used ENM<sup>13,46–48</sup>. We first extracted C $^\alpha$  atoms of amino acids as nodes and connected them with springs if the separating distance lies within the prescribed cutoff distance  $r_c$ . The potential energy of ANM is given by the sum of pairwise harmonic potentials:

$$V(\mathbf{q}) = \frac{1}{2} \sum_{\alpha, \beta} \gamma_{\alpha\beta} \left( r_{\alpha\beta} - r_{\alpha\beta}^o \right)^2 \quad (13)$$

where  $\gamma_{\alpha\beta}$  is the spring force constant between  $i, j$  pair of atoms;  $r_{\alpha\beta} = \|\mathbf{q}_\beta - \mathbf{q}_\alpha\|$  and  $r_{\alpha\beta}^o = \|\mathbf{q}_\beta^o - \mathbf{q}_\alpha^o\|$  are the instantaneous distance and the equilibrium distance between two atoms, respectively. Here we use greek letters as indices to avoid confusion with the indices of individual components used in equation (2). The components in the Hessian of ANM  $\mathbf{H}$  can be obtained from the second derivatives with respect to the components of  $\alpha$  and  $\beta$  atoms:

$$\frac{\partial^2 V}{\partial x_\alpha \partial y_\beta} = -\frac{\gamma_{\alpha\beta}}{r_{\alpha\beta}^2} (x_\beta - x_\alpha) (y_\beta - y_\alpha) \frac{r_{\alpha\beta}^o}{r_{\alpha\beta}} \quad (14)$$

where  $x, y$  are free indices interchangeable with respect to the three dimensions of coordinates. Evaluating equation (14) at equilibrium conformation  $\mathbf{q}_\alpha^o, \mathbf{q}_\beta^o$  yields the off-diagonal Hessian submatrices

$$\mathbf{H}_{\alpha\beta} = -\frac{\gamma_{\alpha\beta}}{r_{\alpha\beta}^2} \begin{bmatrix} (x_\beta^o - x_\alpha^o)^2 & (x_\beta^o - x_\alpha^o)(y_\beta^o - y_\alpha^o) & (x_\beta^o - x_\alpha^o)(z_\beta^o - z_\alpha^o) \\ (x_\beta^o - x_\alpha^o)(y_\beta^o - y_\alpha^o) & (y_\beta^o - y_\alpha^o)^2 & (y_\beta^o - y_\alpha^o)(z_\beta^o - z_\alpha^o) \\ (x_\beta^o - x_\alpha^o)(z_\beta^o - z_\alpha^o) & (y_\beta^o - y_\alpha^o)(z_\beta^o - z_\alpha^o) & (z_\beta^o - z_\alpha^o)^2 \end{bmatrix} \quad (15)$$

and the diagonal Hessian submatrices

$$\mathbf{H}_{\alpha\alpha} = - \sum_{\beta \in \mathcal{N}(\alpha) \setminus \alpha} \mathbf{H}_{\beta\alpha} \quad (16)$$

. The spring force constants  $\gamma_{\alpha\beta}$  are set as 1 in this work.

To elucidate the dynamic behavior of proteins about the equilibrium conformation and find out the underlying cooperative motions, it is of interest to know the cross-correlations between residue fluctuations given by the mode shapes, *i.e.* the eigenvectors of the Hessian, within and across different normal modes. To this end, we can calculate the ensemble average of cross-correlations between certain components of eigenvectors

$$\langle \Delta q_i \Delta q_j \rangle = \frac{1}{Z} \int d^{3N} q e^{-\frac{\Delta \mathbf{q}^T \mathbf{H} \Delta \mathbf{q}}{2k_B T}} \Delta q_i \Delta q_j = k_B T [\mathbf{H}^{-1}]_{ij} \quad (17)$$

where  $Z$  is the configurational integral

$$Z = \int d^{3N} q e^{-\frac{\Delta \mathbf{q}^T \mathbf{H} \Delta \mathbf{q}}{2k_B T}} = (2\pi k_B T)^{\frac{3N}{2}} [\det(\mathbf{H}^{-1})]^{\frac{1}{2}} \quad (18)$$

, and  $[\mathbf{H}^{-1}]_{ij}$  is the  $i, j$ -th element in the inverse of Hessian. The integration performs over the entire configurational space following Boltzmann distribution and therefore favors low energy modes with high probability over high energy modes. By equation (10), the inverse of Hessian can be expressed as

$$\begin{aligned} \tilde{\mathbf{H}} &= \tilde{\mathbf{U}} \Lambda \tilde{\mathbf{U}}^T \\ \tilde{\mathbf{H}}^{-1} &= (\tilde{\mathbf{U}} \Lambda \tilde{\mathbf{U}}^T)^{-1} = (\tilde{\mathbf{U}}^T)^{-1} \Lambda^{-1} \tilde{\mathbf{U}}^{-1} = \tilde{\mathbf{U}} \Lambda^{-1} \tilde{\mathbf{U}}^T \end{aligned}$$

. Since there are six degenerate modes with zero eigenvalues, the inverse of Hessian is replaced by the *pseudoinverse*, which takes the sum of non-degenerate modes

$$\tilde{\mathbf{H}}^{-1} = \sum_{k=1}^{3N-6} \frac{\tilde{\mathbf{u}}^{(k)} (\tilde{\mathbf{u}}^{(k)})^T}{\omega_k^2} \quad (19)$$

. Therewith we have the cross-correlation matrix that is the product of inverse eigenvalues and eigenvectors

by transforming it into the Cartesian coordinates

$$\mathbf{C} = k_B T \mathbf{H}^{-1} = k_B T \sum_{k=1}^{3N-6} \frac{\mathbf{u}^{(k)} \left( \mathbf{u}^{(k)} \right)^\top}{\omega_k^2} \quad (20)$$

. It should be noted that  $\mathbf{C}$  has size of  $3N \times 3N$  and gives the cross-correlation between the individual components of atom coordinates. We therefore reduce it into  $N \times N$  matrix  $\mathbf{c}$  by taking the trace of the  $3 \times 3$  submatrices of  $\mathbf{C}$ , which is equivalent to the sum of the inner products of eigenvectors between  $i, j$  residues:

$$c_{ij} = k_B T \text{tr} \left( \sum_{k=1}^{3N-6} \frac{\mathbf{u}_i^{(k)} \left( \mathbf{u}_j^{(k)} \right)^\top}{\omega_k^2} \right) = k_B T \sum_{k=1}^{3N-6} \frac{\left( \mathbf{u}_i^{(k)} \right)^\top \mathbf{u}_j^{(k)}}{\omega_k^2} \quad (21)$$

Note that all elements of cross-correlation matrix  $\mathbf{c}$  are linearly proportional to  $k_B T$  and thus can be canceled out after normalization with respect to each residues. We therefore reach our final normalized cross-correlation matrix (correlation map)

$$\bar{c}_{ij} = \frac{c_{ij}}{\sqrt{c_{ii}c_{jj}}} \quad (22)$$

such that all of the diagonal elements are equal to 1 and off-diagonal elements represent the normalized correlation between residues.

## Persistent homology (PH)

Persistent homology (PH) is an algebraic topology method for measuring topological features of shapes, data, and functions<sup>28,49</sup>. It provides a stable tool for a myriad of applications, including biomolecules classification, geometric modeling, and network analysis.

Consider the union of identical  $\varepsilon$ -balls around  $C^\alpha$  atoms. The simplicial complex (points, lines, triangles, and tetrahedra) of  $C^\alpha$  atoms start to emerge and then disappear (birth and death of  $k$ -simplices) as the radii of the balls increase. The nested sequence of this simplicial complex is the *filtration* filtered by the radius of the ball. Each birth-death pair is then transformed into the *persistence diagram* (PD) by mapping to birth-persistence coordinate. The vertical distance between diagonal line and point is exactly the persistence of the topological feature. We used *alpha complex* to compute the one- and two-dimensional

persistent homology group  $H_1, H_2$ . For a given  $\alpha$ , the alpha complex includes all the simplices in Delaunay triangulation which have an empty circumscribing ball with squared radius equal or smaller than  $\alpha$ . The filtration of alpha complex therefore allows us to extract the topological features of loops and cavities in protein structures.

## Persistence images (PI)

Let  $D$  be a PD in birth-death coordinates and  $T : \mathbb{R}^2 \rightarrow \mathbb{R}^2$  be the linear transformation  $T(x_1, x_2) = (x_1, x_2 - x_1)$  from birth-death coordinates to birth-persistence coordinates. At each transformed point  $\mathbf{u} = (u_1, u_2) = (x_1, x_2 - x_1) \in T(D)$  we placed a Gaussian kernel function

$$\phi_{\mathbf{u}, \sigma^2}(\mathbf{z}) = \frac{1}{2\pi\sigma^2} e^{-\frac{(z_1 - u_1)^2 + (z_2 - u_2)^2}{2\sigma^2}} \quad (23)$$

where  $\sigma^2$  is the variance of the gaussian kernel. With an appropriate weighting function  $w : \mathbb{R}^2 \rightarrow \mathbb{R}$ , we transform PD into the *persistence surface*

$$\rho_D(\mathbf{z}) = \sum_{\mathbf{u} \in T(D)} w(\mathbf{u}) \phi_{\mathbf{u}, \sigma^2}(\mathbf{z}) \quad (24)$$

. We designate  $\sigma^2 = 1$  and  $w$  as the square of persistence

$$w(\mathbf{u}) = u_2^2 = (x_2 - x_1)^2 \quad (25)$$

. The function intensifies the feature with larger persistence and satisfies stability requirements being zero along  $z_1$ , continuous, and piecewise differentiable<sup>28</sup>. By taking the pixel-wise integral of the discretized persistence surface, we obtain the *persistence image* (PI) consisting of a vector of integral value for each pixel  $p$

$$I(\rho_D)_p = \iint_p \rho_D dx dy \quad (26)$$

. Throughout this work, we transform the identical PD domains within  $[0, 50] \times [0, 50]$  into PIs of size  $25 \times 25$ , namely vectors of 625 dimensions. The choices of image resolution, kernel probability distribution, as well as weighting functions may vary for different tasks at hands and should be left as an open question

to select the optimal ones. However, previous experimental studies have indicated that the classification accuracy in machine learning framework is robust against the choice of image resolution<sup>28,50</sup> and has low sensitivity to the variance of Gaussian kernel (equation (23)). The implementation of persistent homology and persistence image representation were carried out using GUDHI library with CGAL as the backend for alpha complex calculation<sup>51,52</sup>.

## Datasets and training configurations

Our dataset consists of 7,765 proteins and 155 Gene Ontology (GO) annotations retrieved from Protein Data Bank (PDB)<sup>5,21–24</sup> and Structure Integration with Function, Taxonomy, and Sequence (SIFTS) database<sup>21,25,26</sup>. The 3D atomic structures of proteins are collected based on the size and resolution. We filtered out proteins larger than 5,000 deposited atoms excluding water molecules, and selected the proteins starting from the highest structure resolution. Among approximate 110,000 legitimate protein candidates, the first 10,000 proteins sorted by resolution were first selected, with 7,765 of them (which have valid PDB, contact maps, and SIFTS MF-GO annotations) retrieved through ProDy package<sup>53,54</sup>. ProDy is a protein structural and dynamical analysis tool streaming multiple resources of PDBs affiliated with World Wide Protein Data Bank (wwPDB)<sup>5,21–24</sup>. Among 7,765 proteins, 6,989 of them are used for training and validation, and the remaining 776 proteins are used for testing. 3D protein structures are visualized by PyMOL<sup>55</sup> and VMD<sup>56</sup> in this work. We trained our model to predict the MF-GO annotations that have enough training samples. The MF-GO terms that annotate less than 25 PDB entries are excluded from our dataset.

To optimize the multi-label classification prediction and take the imbalanced samples into account, all models were trained to minimize the weighted cross-entropy loss function that induces models to act if the balanced samples are given:

$$\mathcal{L} = -\frac{1}{NL} \sum_{i=1}^N \sum_{j=1}^L w_j y_{ij} \log(\hat{y}_{ij}) + (1 - y_{ij}) \log(1 - \hat{y}_{ij}) \quad (27)$$

where  $N$  is the total number of training samples,  $L$  is the number of MF-GO classes,  $y_{ij}$  is the true binary indicator for protein  $i$  to have MF-GO function  $j$ , and  $\hat{y}_{ij}$  is the predicted probability that protein  $i$  is annotated with MF-GO function  $j$ ;  $w_j$  is the added weight for the positive class  $j$ , which is assigned as the

ratio between negative and positive samples

$$w_j = \frac{n_j^-}{n_j^+} \quad (28)$$

For inference prediction, the protein  $i$  is said to have function  $j$  annotated with associated GO terms if the predicted probability  $\hat{y}_{ij} \geq 0.5$ . True positive rate (TPR), true negative rate (TNR), false positive rate (FPR), and false negative rate (FNR) are calculated by varying the threshold value from 0 to 1 to obtain the precision-recall curve.

We randomly separated our dataset into train and test set by 90% and 10%. We used ADAM optimizer<sup>57</sup> with learning rate  $LR = 5 \times 10^{-5}$  and exponential decay rate  $\beta_1 = 0.9, \beta_2 = 0.999$ . To avoid overfitting, we employed weight decay  $1 \times 10^{-5}$ <sup>58</sup> and further applied dropout regularization  $p = 0.1$  and layer normalization after each linear layer<sup>59</sup>. Each model is trained for 300 epochs with batch size of 64 on NVIDIA V100 16/32G GPU. The model training is implemented using PyTorch deep learning library<sup>60</sup>.

## Residue-level activation map and saliency difference $\Delta$ SALS

To locate the residues crucial for protein function, we devised a method inspired by Gradient-weighted Class Activation Map (Grad-CAM)<sup>17,27</sup> to find the residues with highest contribution at inference stage. Motivated by its recent success in image classification and residue-level annotations for proteins, we used Grad-CAM to identify the residues that are important for function prediction. The method produces visual explanation from neural network and highlights the features that contribute more to the activation in the downstream neurons.

We used PyTorch hook to extract the residue embeddings after each graph convolutional layer  $\mathbf{H}^{(k)} \in \mathbb{R}^{V \times D_k}$ . To compute the contribution of each residue  $i$  to the prediction of function  $j$ , we computed derivatives of the model output layer  $\hat{y}_j$  with respect to residue embeddings  $\mathbf{h}_i^{(k)} \in \mathbb{R}^{D_k}$ :

$$\alpha_i^j = \frac{\partial \hat{y}_j}{\partial \mathbf{h}_i} \quad (29)$$

where  $\alpha^j$  measures the importance of each feature in residue embeddings for predicting function  $j$ . Instead of summing the derivatives from individual residue for measuring the importance of a specific feature map

$\mathbf{f}_c \in \mathbb{R}^V$  (*i.e.*  $c$  channel of residue embeddings along residue space  $\mathbf{H}^{(k)} = [\mathbf{f}_1, \dots, \mathbf{f}_{D_k}] = [\mathbf{h}_1, \dots, \mathbf{h}_V]^T$ ) as implemented by Gligorijević *et al.*<sup>17</sup>, here we maintained the vector form of feature map and took its inner product with the importance vector for each residue to obtain the function-specific heatmap in the residue space:

$$\text{CAM}_i^j = \text{ReLU}(\alpha_i^j \cdot \mathbf{h}_i) = \text{ReLU}\left(\sum_{c=1}^{D_k} \alpha_{ic}^j h_{ic}\right) \quad (30)$$

where ReLU function ensures that only positive contributions to the function prediction are preserved.

The difference of saliency map is given by:

$$\Delta\text{SALS} = \text{SALS}^{\text{ContactCorr}} - \text{SALS}^{\text{Contact}} \quad (31)$$

$$\text{SALS}_i = \sum_{j=1}^V |I_j - I_i| \quad (32)$$

where  $I_j$  is the intensity of activation signal at residue  $j, \forall j \in \mathcal{V}$ . The saliency map accentuates the region that is noticeable among its neighborhood, providing a self-referential measure of feature importance such that the comparison between the Grad-CAM from ContactCorr network and the vanilla one from Contact network becomes meaningful. The difference of saliency map  $\Delta\text{SALS}$  therefore identifies the residues that are confidently activated or suppressed by the ContactCorr network compared with Contact network.

## Acknowledgements

The authors appreciate the financial support from the Ministry of Science and Technology, Taiwan [109-2224-E-007-003, 110-2636-E-002-013]. We thank National Center for High-performance Computing (NCHC) for providing computational and storage resources.

## Author Contributions

Y.C. and S.W.C. conceived the research ideas; Y.C. designed, developed, and trained the deep learning model; W.H.H. performed the molecular dynamics simulation; Y.C. analyzed the simulation results; Y.C. wrote the paper with input and advice from S.W.C.

## Declaration of Interests

The authors declare no competing interests.

## Computer Code

The code implementation associated with this paper is publicly available on GitHub (<https://github.com/Chiang-Yuan/ProDAR>)

## References

- [1] Jan Drenth. *Principles of protein X-ray crystallography*. Springer Science & Business Media, 2007.
- [2] Xiao-Chen Bai, Greg McMullan, and Sjors HW Scheres. How cryo-em is revolutionizing structural biology. *Trends in biochemical sciences*, 40(1):49–57, 2015.
- [3] Radostin Danev, Haruaki Yanagisawa, and Masahide Kikkawa. Cryo-electron microscopy methodology: current aspects and future directions. *Trends in biochemical sciences*, 44(10):837–848, 2019.
- [4] Shigeyuki Matsumoto, Shoichi Ishida, Mitsugu Araki, Takayuki Kato, Kei Terayama, and Yasushi Okuno. Extraction of protein dynamics information from cryo-em maps using deep learning. *Nature Machine Intelligence*, 3(2):153–160, 2021.
- [5] Helen Berman, Kim Henrick, and Haruki Nakamura. Announcing the worldwide protein data bank. *Nature Structural & Molecular Biology*, 10(12):980–980, 2003.
- [6] Uniprot: the universal protein knowledgebase in 2021. *Nucleic Acids Research*, 49(D1):D480–D489, 2021.
- [7] Benjamin Webb and Andrej Sali. Comparative protein structure modeling using modeller. *Current protocols in bioinformatics*, 54(1):5–6, 2016.
- [8] Andrew Waterhouse, Martino Bertoni, Stefan Bienert, Gabriel Studer, Gerardo Tauriello, Rafal Gummienny, Florian T Heer, Tjaart A P de Beer, Christine Rempfer, Lorenza Bordoli, et al. Swiss-model:

homology modelling of protein structures and complexes. *Nucleic acids research*, 46(W1):W296–W303, 2018.

- [9] John Jumper, Richard Evans, Alexander Pritzel, Tim Green, Michael Figurnov, Olaf Ronneberger, Kathryn Tunyasuvunakool, Russ Bates, Augustin Žídek, Anna Potapenko, et al. Highly accurate protein structure prediction with alphafold. *Nature*, pages 1–11, 2021.
- [10] Minkyung Baek, Frank DiMaio, Ivan Anishchenko, Justas Dauparas, Sergey Ovchinnikov, Gyu Rie Lee, Jue Wang, Qian Cong, Lisa N Kinch, R Dustin Schaeffer, et al. Accurate prediction of protein structures and interactions using a three-track neural network. *Science*, 2021.
- [11] Fabian B Fuchs, Daniel E Worrall, Volker Fischer, and Max Welling. Se (3)-transformers: 3d rotation equivariant attention networks. *arXiv preprint arXiv:2006.10503*, 2020.
- [12] John Ingraham, Vikas K Garg, Regina Barzilay, and Tommi Jaakkola. Generative models for graph-based protein design. 2019.
- [13] Ivet Bahar, Timothy R Lezon, Ahmet Bakan, and Indira H Shrivastava. Normal mode analysis of biomolecular structures: functional mechanisms of membrane proteins. *Chemical reviews*, 110(3):1463–1497, 2010.
- [14] Shaimaa Waz, Teruya Nakamura, Keisuke Hirata, Yukari Koga-Ogawa, Mami Chirifu, Takao Arimori, Taro Tamada, Shinji Ikemizu, Yusaku Nakabeppu, and Yuriko Yamagata. Structural and kinetic studies of the human nudix hydrolase mth1 reveal the mechanism for its broad substrate specificity. *Journal of biological chemistry*, 292(7):2785–2794, 2017.
- [15] Da Chen Emily Koo and Richard Bonneau. Towards region-specific propagation of protein functions. *Bioinformatics*, 35(10):1737–1744, 2019.
- [16] Sayoni Das, Harry M Scholes, Neeladri Sen, and Christine Orengo. Cath functional families predict functional sites in proteins. *Bioinformatics*, 37(8):1099–1106, 2021.
- [17] Vladimir Gligorijević, P Douglas Renfrew, Tomasz Kosciolk, Julia Koehler Leman, Daniel Berenberg, Tommi Vatanen, Chris Chandler, Bryn C Taylor, Ian M Fisk, Hera Vlamakis, et al. Structure-

- based protein function prediction using graph convolutional networks. *Nature communications*, 12(1):1–14, 2021.
- [18] Amelia Villegas-Morcillo, Stavros Makrodimitris, Roeland CHJ van Ham, Angel M Gomez, Victoria Sanchez, and Marcel JT Reinders. Unsupervised protein embeddings outperform hand-crafted sequence and structure features at predicting molecular function. *Bioinformatics*, 37(2):162–170, 2021.
- [19] Soumya Sanyal, Ivan Anishchenko, Anirudh Dagar, David Baker, and Partha Talukdar. Proteingcn: Protein model quality assessment using graph convolutional networks. *bioRxiv*, 2020.
- [20] Nicolas Swenson, Aditi S Krishnapriyan, Aydin Buluc, Dmitriy Morozov, and Katherine Yelick. Persgnn: Applying topological data analysis and geometric deep learning to structure-based protein function prediction. *arXiv preprint arXiv:2010.16027*, 2020.
- [21] Saqib Mir, Younes Alhroub, Stephen Anyango, David R Armstrong, John M Berrisford, Alice R Clark, Matthew J Conroy, Jose M Dana, Mandar Deshpande, Deepti Gupta, et al. Pdbe: towards reusable data delivery infrastructure at protein data bank in europe. *Nucleic acids research*, 46(D1):D486–D492, 2018.
- [22] Stephen K Burley, Charmi Bhikadiya, Chunxiao Bi, Sebastian Bittrich, Li Chen, Gregg V Crichlow, Cole H Christie, Kenneth Dalenberg, Luigi Di Costanzo, Jose M Duarte, et al. Rcsb protein data bank: powerful new tools for exploring 3d structures of biological macromolecules for basic and applied research and education in fundamental biology, biomedicine, biotechnology, bioengineering and energy sciences. *Nucleic acids research*, 49(D1):D437–D451, 2021.
- [23] Akira R Kinjo, Gert-Jan Bekker, Hirofumi Suzuki, Yuko Tsuchiya, Takeshi Kawabata, Yasuyo Ikegawa, and Haruki Nakamura. Protein data bank japan (pdbj): updated user interfaces, resource description framework, analysis tools for large structures. *Nucleic acids research*, page gkw962, 2016.
- [24] Akira R Kinjo, Gert-Jan Bekker, Hiroshi Wako, Shigeru Endo, Yuko Tsuchiya, Hiromu Sato, Hafumi

- Nishi, Kengo Kinoshita, Hirofumi Suzuki, Takeshi Kawabata, et al. New tools and functions in data-out activities at protein data bank japan (pdbj). *Protein Science*, 27(1):95–102, 2018.
- [25] Sameer Velankar, José M Dana, Julius Jacobsen, Glen Van Ginkel, Paul J Gane, Jie Luo, Thomas J Oldfield, Claire O’Donovan, Maria-Jesus Martin, and Gerard J Kleywegt. Sifts: structure integration with function, taxonomy and sequences resource. *Nucleic acids research*, 41(D1):D483–D489, 2012.
- [26] Jose M Dana, Aleksandras Gutmanas, Nidhi Tyagi, Guoying Qi, Claire O’Donovan, Maria Martin, and Sameer Velankar. Sifts: updated structure integration with function, taxonomy and sequences resource allows 40-fold increase in coverage of structure-based annotations for proteins. *Nucleic acids research*, 47(D1):D482–D489, 2019.
- [27] Ramprasaath R Selvaraju, Michael Cogswell, Abhishek Das, Ramakrishna Vedantam, Devi Parikh, and Dhruv Batra. Grad-cam: Visual explanations from deep networks via gradient-based localization. In *Proceedings of the IEEE international conference on computer vision*, pages 618–626, 2017.
- [28] Herbert Edelsbrunner, John Harer, et al. Persistent homology-a survey. *Contemporary mathematics*, 453:257–282, 2008.
- [29] Henry Adams, Tegan Emerson, Michael Kirby, Rachel Neville, Chris Peterson, Patrick Shipman, Sofya Chepushtanova, Eric Hanson, Francis Motta, and Lori Ziegelmeier. Persistence images: A stable vector representation of persistent homology. *Journal of Machine Learning Research*, 18, 2017.
- [30] Thomas N Kipf and Max Welling. Semi-supervised classification with graph convolutional networks. *arXiv preprint arXiv:1609.02907*, 2016.
- [31] William L Hamilton, Rex Ying, and Jure Leskovec. Inductive representation learning on large graphs. In *Proceedings of the 31st International Conference on Neural Information Processing Systems*, pages 1025–1035, 2017.
- [32] Karsten M Borgwardt, Cheng Soon Ong, Stefan Schönauer, SVN Vishwanathan, Alex J Smola, and Hans-Peter Kriegel. Protein function prediction via graph kernels. *Bioinformatics*, 21(suppl\_1): i47–i56, 2005.

- [33] Keyulu Xu, Weihua Hu, Jure Leskovec, and Stefanie Jegelka. How powerful are graph neural networks? *arXiv preprint arXiv:1810.00826*, 2018.
- [34] Wen Torng and Russ B Altman. High precision protein functional site detection using 3d convolutional neural networks. *Bioinformatics*, 35(9):1503–1512, 2019.
- [35] Kristoffer Forslund and Erik LL Sonnhammer. Predicting protein function from domain content. *Bioinformatics*, 24(15):1681–1687, 2008.
- [36] Bolei Zhou, Aditya Khosla, Agata Lapedriza, Aude Oliva, and Antonio Torralba. Learning deep features for discriminative localization. In *Proceedings of the IEEE conference on computer vision and pattern recognition*, pages 2921–2929, 2016.
- [37] Estelle M Maes, Andrzej Weichsel, John F Andersen, Donald Shepley, and William R Montfort. Role of binding site loops in controlling nitric oxide release: structure and kinetics of mutant forms of nitrophorin 4. *Biochemistry*, 43(21):6679–6690, 2004.
- [38] Alexandra C Walls, Young-Jun Park, M Alejandra Tortorici, Abigail Wall, Andrew T McGuire, and David Veessler. Structure, function, and antigenicity of the sars-cov-2 spike glycoprotein. *Cell*, 181(2):281–292, 2020.
- [39] Jun Lan, Jiwan Ge, Jinfang Yu, Sisi Shan, Huan Zhou, Shilong Fan, Qi Zhang, Xuanling Shi, Qisheng Wang, Linqi Zhang, et al. Structure of the sars-cov-2 spike receptor-binding domain bound to the ace2 receptor. *Nature*, 581(7807):215–220, 2020.
- [40] Lili Wu, Qian Chen, Kefang Liu, Jia Wang, Pengcheng Han, Yanfang Zhang, Yu Hu, Yumin Meng, Xiaoqian Pan, Chengpeng Qiao, et al. Broad host range of sars-cov-2 and the molecular basis for sars-cov-2 binding to cat ace2. *Cell discovery*, 6(1):1–12, 2020.
- [41] Yuan Yuan, Duanfang Cao, Yanfang Zhang, Jun Ma, Jianxun Qi, Qihui Wang, Guangwen Lu, Ying Wu, Jinghua Yan, Yi Shi, et al. Cryo-em structures of mers-cov and sars-cov spike glycoproteins reveal the dynamic receptor binding domains. *Nature communications*, 8(1):1–9, 2017.

- [42] HU Mei, Zhi H Liao, Yuan Zhou, and Shengshi Z Li. A new set of amino acid descriptors and its application in peptide qsars. *Peptide Science: Original Research on Biomolecules*, 80(6):775–786, 2005.
- [43] Sean R Eddy. Where did the blosum62 alignment score matrix come from? *Nature biotechnology*, 22(8):1035–1036, 2004.
- [44] Tristan Bepler and Bonnie Berger. Learning protein sequence embeddings using information from structure. *arXiv preprint arXiv:1902.08661*, 2019.
- [45] Hesham ElAbd, Yana Bromberg, Adrienne Hoarfrost, Tobias Lenz, Andre Franke, and Mareike Wendorff. Amino acid encoding for deep learning applications. *BMC bioinformatics*, 21(1):1–14, 2020.
- [46] Monique M Tirion. Large amplitude elastic motions in proteins from a single-parameter, atomic analysis. *Physical review letters*, 77(9):1905, 1996.
- [47] Ali Rana Atilgan, SR Durell, Robert L Jernigan, Melik C Demirel, O Keskin, and Ivet Bahar. Anisotropy of fluctuation dynamics of proteins with an elastic network model. *Biophysical journal*, 80(1):505–515, 2001.
- [48] Eran Eyal, Lee-Wei Yang, and Ivet Bahar. Anisotropic network model: systematic evaluation and a new web interface. *Bioinformatics*, 22(21):2619–2627, 2006.
- [49] Herbert Edelsbrunner and John Harer. *Computational topology: an introduction*. American Mathematical Soc., 2010.
- [50] Matthias Zeppelzauer, Bartosz Zieliński, Mateusz Juda, and Markus Seidl. Topological descriptors for 3d surface analysis. In *International Workshop on Computational Topology in Image Context*, pages 77–87. Springer, 2016.
- [51] Clément Maria, Jean-Daniel Boissonnat, Marc Glisse, and Mariette Yvinec. The gudhi library: Simplicial complexes and persistent homology. In *International congress on mathematical software*, pages 167–174. Springer, 2014.

- [52] Tran Kai Frank Da, Sébastien Lorient, and Mariette Yvinec. 3D alpha shapes. In *CGAL User and Reference Manual*. CGAL Editorial Board, 5.3 edition, 2021. URL <https://doc.cgal.org/5.3/Manual/packages.html#PkgAlphaShapes3>.
- [53] Ahmet Bakan, Lidio M Meireles, and Ivet Bahar. Prody: protein dynamics inferred from theory and experiments. *Bioinformatics*, 27(11):1575–1577, 2011.
- [54] Peter JA Cock, Tiago Antao, Jeffrey T Chang, Brad A Chapman, Cymon J Cox, Andrew Dalke, Iddo Friedberg, Thomas Hamelryck, Frank Kauff, Bartek Wilczynski, et al. Biopython: freely available python tools for computational molecular biology and bioinformatics. *Bioinformatics*, 25(11):1422–1423, 2009.
- [55] Schrödinger, LLC. The PyMOL molecular graphics system, version 1.8. November 2015.
- [56] William Humphrey, Andrew Dalke, and Klaus Schulten. Vmd: visual molecular dynamics. *Journal of molecular graphics*, 14(1):33–38, 1996.
- [57] Diederik P Kingma and Jimmy Ba. Adam: A method for stochastic optimization. *arXiv preprint arXiv:1412.6980*, 2014.
- [58] Ilya Loshchilov and Frank Hutter. Decoupled weight decay regularization. *arXiv preprint arXiv:1711.05101*, 2017.
- [59] Jimmy Lei Ba, Jamie Ryan Kiros, and Geoffrey E Hinton. Layer normalization. *arXiv preprint arXiv:1607.06450*, 2016.
- [60] Adam Paszke, Sam Gross, Soumith Chintala, Gregory Chanan, Edward Yang, Zachary DeVito, Zeming Lin, Alban Desmaison, Luca Antiga, and Adam Lerer. Automatic differentiation in pytorch. 2017.